

CHAPTER IV

Results

Results presented in this chapter will be divided into two sections. Section 4.1 shows the verification tests, an important step in which analytical solutions are used in order to verify the correctness of the code implementation. Section 4.2 shows the results of the simulation of bubble flows.

4.1 Verification

The verification procedure will be applied separately to the Navier-Stokes solver and the front-tracking tools. Both are based on the Method of Manufactured Solutions (MMS) (ROACHE, 1998), which consists in using analytical functions to set up initial and boundary conditions, as well as source terms when necessary, so that the numerical solution can be compared to analytical functions and the quality of the solution can be verified. One of the few requirements on these functions is that they must satisfy the physical constraints of the problem that will be simulated by the computational code under test. In the case of a Navier-Stokes solver, the velocity field must be solenoidal and, for multiphase flows, density and viscosity fields must not have a constant value.

4.1.1 Navier-Stokes solver

Let $r(x, y, z, t) = \pi(w_1x + w_2y + w_3z) + w_4t$, where w_i are constants. The analytical expressions for the velocity, pressure, density and viscosity fields are given by (SILVA; VILLAR, 2010):

$$u_e = \sin^2(r), \quad (4.1)$$

$$v_e = -\cos^2(r), \quad (4.2)$$

$$w_e = \frac{w_1 + w_2}{w_3} \cos^2(r), \quad (4.3)$$

$$p_e = \cos^2(r), \quad (4.4)$$

$$\rho_e = 1 + 0.1 \sin^2(r), \quad (4.5)$$

$$\mu_e = 1 + 0.2 \cos^2(r). \quad (4.6)$$

where the subscript e stands for the manufactured exact solutions of the primary variables. Notice that the velocity profile given by eqs. 4.1 - 4.3 is solenoidal. Parameters w_i are used in order to choose which term will be active in the expression for $r(x, y, z, t)$. Here, $w_1 = w_2 = w_3 = 2$, $w_4 = 1$. The expression for the source term is obtained by isolating the external force term in the momentum equation, in a procedure similar to Villar (2007), who employed MMS in a two-dimensional version of the present AMR code.

The computational domain is a unitary cube and the time step is calculated dynamically, based on the stability criteria given by Eq. (3.16). Figure (4.1) shows an example of the mesh employed in the simulations, displaying the boundaries of each refinement level. Although it is locally refined, it will not dynamically change in time (static AMR).

For a mesh with grid spacing Δx , Δy and Δz at the x-, y- and z-directions and characteristic length $h = \min(\Delta x, \Delta y, \Delta z)$, the refinement ratio r is defined as the quotient between the characteristic length of the current level and the characteristic length of the subsequent refined level. In this work, a constant ratio $r = 2$ was used in all simulations.

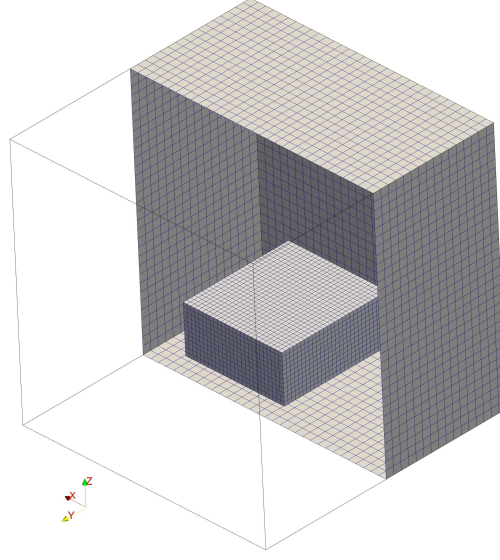


Figure 4.1: Static grid with one refinement level used on the convergence rate analysis.

The error between the numerical and exact solutions is quantified using the L_2 -norm:

$$\Phi^h(\phi) = L_2^h(\phi) = \sqrt{\frac{1}{V_\Omega} \sum_{i \in \Omega_u^h} (\phi_i - \phi_i^e)^2 w_i} \quad (4.7)$$

where V_Ω is the volume of the Eulerian domain and the weights w_i are given by:

$$w_i = \begin{cases} \Delta x \Delta y \Delta z, & \text{on the coarse grid} \\ \frac{\Delta x \Delta y \Delta z}{r^3}, & \text{on the fine grid} \\ \left(\frac{r+1}{2}\right) \left(\frac{\Delta x \Delta y \Delta z}{r^3}\right) & \text{at the coarse-fine grid interface} \end{cases} \quad (4.8)$$

The convergence rate is

$$\varepsilon = \log_2 \left(\frac{\Phi^{2h}}{\Phi^h} \right). \quad (4.9)$$

An analysis of spacial convergence rate was performed. The coarsest mesh has a characteristic length $h = 1/16$, and the subsequent meshes are refined with a constant refinement ratio $r = 2$, leaving the sizes of the patches unchanged.

Three sets of cases were run, based on the kind of boundary conditions applied:

1. Dirichlet for the velocity and Neumann for the pressure,
2. Neumann for the velocity and Dirichlet for the pressure,
3. Periodicity for both variables.

Table (4.1) shows the errors and the convergence rate obtained for case 1. As expected, a second order rate was achieved for the velocity, while the pressure yielded a rate between 1 and 2 (VILLAR, 2007).

Table 4.1: Verification tests. Navier Stokes solver run with Dirichlet boundary conditions for velocity and Neumann for the pressure.

convergence rate test: L_2 -norm of error and convergence rate (ϵ)							
	$L_2(h_1)$	ϵ_1	$L_2(h_2)$	ϵ_2	$L_2(h_3)$	ϵ_3	$L_2(h_4)$
u	1.6921×10^{-2}	1.98	4.2792×10^{-3}	1.98	1.0861×10^{-3}	1.99	2.7372×10^{-4}
v	1.6916×10^{-2}	1.98	4.2723×10^{-3}	1.98	1.0846×10^{-3}	1.99	2.7374×10^{-4}
w	3.2330×10^{-2}	1.99	8.1525×10^{-3}	1.99	2.0590×10^{-3}	2.00	5.1586×10^{-4}
p	7.9853×10^{-1}	1.77	2.3485×10^{-1}	1.79	6.8130×10^{-2}	1.78	1.9900×10^{-2}

A comparison between this case and tables 4.1 and 4.2 shows that the velocity field is less sensitive to the grid refinement when Dirichlet boundary conditions are applied. Also, Neumann and Periodic boundary conditions yielded slightly higher error values when compared to the case with Dirichlet boundary conditions applied on the velocity field.

Table 4.2: Verification tests. Navier Stokes solver run with Neumann boundary conditions for velocity and Dirichlet for the pressure.

convergence rate test: L_2 -norm of error and convergence rate (ϵ)							
	$L_2(h_1)$	ϵ_1	$L_2(h_2)$	ϵ_2	$L_2(h_3)$	ϵ_3	$L_2(h_4)$
u	7.8481×10^{-2}	1.83	2.1946×10^{-2}	2.02	5.4177×10^{-3}	2.00	1.3517×10^{-3}
v	8.3795×10^{-2}	1.91	2.2303×10^{-2}	2.02	5.4880×10^{-3}	1.99	1.3795×10^{-3}
w	1.7025×10^{-1}	1.94	4.4415×10^{-2}	2.03	1.0866×10^{-2}	2.39	2.7032×10^{-3}
p	2.7321×10^{-1}	1.69	8.4886×10^{-2}	1.62	2.7610×10^{-2}	1.60	9.1248×10^{-3}

4.1.2 Front tracking tools

Front tracking tools refer to the framework related to the Lagrangian representation of the interface, as well as the coupling between this framework and the Eulerian Framework in which the Navier-Stokes equations are solved. In this sense, four sets of tests are presented. Firstly, a

Table 4.3: Verification tests. Navier Stokes solver run with Periodic boundary conditions for both, velocity and pressure.

convergence rate test: L_2 -norm of error and convergence rate (ϵ)							
	$L_2(h_1)$	ϵ_1	$L_2(h_2)$	ϵ_2	$L_2(h_3)$	ϵ_3	$L_2(h_4)$
u	8.1853×10^{-2}	1.86	2.2471×10^{-2}	2.02	5.5403×10^{-3}	2.00	1.3821×10^{-3}
v	8.6375×10^{-2}	1.92	2.2782×10^{-2}	2.03	5.5946×10^{-3}	2.00	1.4024×10^{-3}
w	1.7374×10^{-1}	1.94	4.5208×10^{-2}	2.03	1.1073×10^{-2}	2.01	2.7533×10^{-3}
p	2.2650×10^{-1}	1.59	7.5343×10^{-2}	1.54	2.5881×10^{-2}	1.55	8.8417×10^{-3}

simple remeshing test is applied to static meshes in order to assess the effectiveness of the remeshing algorithm in preserving volume and shape of the surface. Secondly, the geometric indicator function is tested by comparing the CPT distance field to the analytical distance field for two analytical surfaces. In the third test, the influence of high aspect ratio elements on the outcome of the indicator function and of the interface force is also assessed. Finally, in the fourth test, an analytical shear flow test is performed, in order to study the influence of various simulation parameters on the volume and shape conservation for a spherical surface.

Volume

This is a simple test which aims at evaluating the ability of the coarsening algorithm provided by GTS on preserving the volume of the geometry discretized by the surface mesh, as well as its ability to keep geometric details, such as corners. Since mesh refinement does not introduce any changes in the surface geometry, its influence was not tested.

The tests were performed on a sphere with unit diameter and on cube with unitary edge. In both cases the volume change was less than $1.0 \times 10^{-11}\%$ relative to the original value. Figures (4.2) and (4.3) show the meshes before and after coarsening for each case. Notice that in the case of the cube, the edges and corners of the surface were fully preserved.

Indicator Function

The idea behind the closest point transform is to find a discrete version of the distance field. When the surface has an analytical representation, CPT is not necessary since all points on the surface are known and the point-to-point distance formula can be used. In this section, the CPT

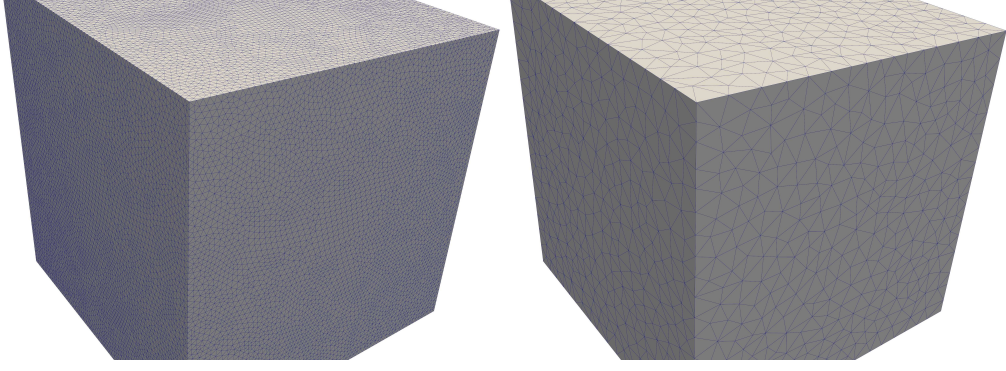


Figure 4.2: Surface mesh of a unit cube before and after mesh coarsening.

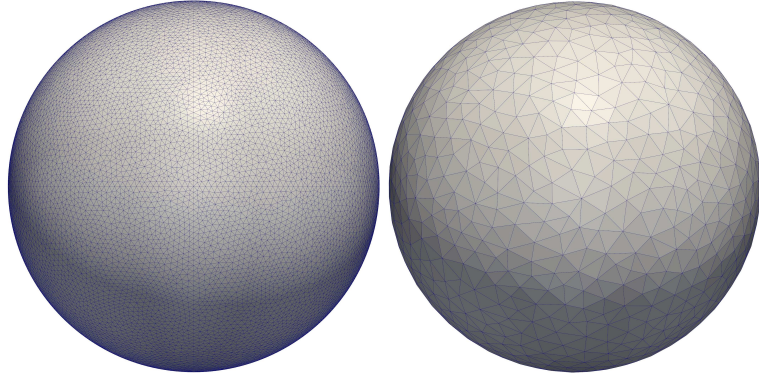


Figure 4.3: Surface mesh of a unit sphere before and after mesh coarsening.

accuracy is tested based on this approach, by measuring the difference between the analytical distance field and the CPT field for a sphere. The expression for the signed distance between a given point P in 3D space and the surface of a sphere S with centre C and radius R is given by

$$d(x, y, z) = \|\mathbf{v}(x, y, z)\| - R \quad (4.10)$$

where $\mathbf{v}(x, y, z) = P - C$ is the vector going from the sphere centre to the point P . When P lies on the surface, $d = 0$. If P lies outside the sphere, $d > 0$ and, if P is inside the sphere, $d < 0$. Therefore, expression 4.10 follows the same sign convention as CPT.

The test was performed based on a sphere with diameter $\phi = 1$ discretized with 3 progressively refined Lagrangian meshes, having characteristic lengths (that is, the mean edge length) $\xi_L = \phi/10$, $\xi_L = \phi/20$ and $\xi_L = \phi/40$. A characteristic length ratio $\lambda_\xi = 2$ was employed, that is, the Eulerian grid and the Lagrangian mesh were refined at the same ratio. The error in the L_∞ -norm yielded values $\varepsilon = 0.16$, $\varepsilon = 0.08$ and $\varepsilon = 0.04$. Figure (4.4) shows the Eulerian cells tagged by the indicator function for the coarsest mesh case. These results shows, therefore, that the closest

point transform yields a first order approximation to the exact signed distance function.

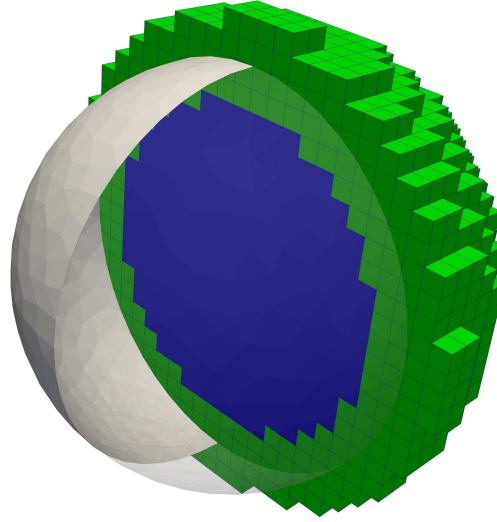


Figure 4.4: Eulerian cells flagged by the indicator function for a spherical geometry.

Analytic Shear Flow.

This test consists in subjecting a surface, usually spherical, to a solenoidal, periodic, analytic velocity field and assessing its volume change as the flow evolves. Assuming a velocity field with a period T , the surface is stretched until $t = T/2$ and then returns to its original position and shape. The velocity field may be calculated either directly on the Lagrangian vertices or interpolated from an auxiliary grid, allowing to assess the influence of the interpolation functions on the volume change during the simulation. Regarding the interface advection, two time integration schemes were assessed: first order Euler method and a second order method based on the trapezoidal rule, respectively Eqs. 3.20 and 3.21.

The velocity profile is given by Eq. (4.11) (SINGH; SHYY, 2007) and the interpolation of the velocity field was performed using Eqs. (3.2), (3.3) and (3.4) (PESKIN, 2002).

$$\begin{aligned}
 u(x,y,z,t) &= \cos(\pi t/T) \sin^2(\pi x) (\sin(2\pi z) - \sin(2\pi y)) \\
 v(x,y,z,t) &= \cos(\pi t/T) \sin^2(\pi y) (\sin(2\pi x) - \sin(2\pi z)) \\
 w(x,y,z,t) &= \cos(\pi t/T) \sin^2(\pi z) (\sin(2\pi y) - \sin(2\pi x))
 \end{aligned}
 \tag{4.11}$$

The sphere diameter is set to $\phi = 0.3m$ and its center is $C(0.5, 0.75, 0.5)m$. In all cases simulated, the characteristic length of the surface mesh, defined as the mean edge length, was set

to $\xi_L = \phi/32$.

Figure (4.5) shows snapshots of an initially spherical shape during a typical simulation at $t = 0$, $t = T/4$, $t = T/2$, $t = 3T/4$ and $t = T$. The period is $T = 4s$, the same which was used in the simulations presented here. The surface is stretched until $T = T/2$ and then ideally would symmetrically return to its initial position, so that the shape and position should be the same not only when comparing $t = 0$ and $t = T$, but also when comparing $t = T/4$ and $t = 3T/4$.



Figure 4.5: Deformation of a spherical surface when subjected to the analytical velocity field given by Eq. (4.11). Snapshots taken at $t = 0$, $t = \frac{T}{4}$, $t = \frac{T}{2}$, $t = \frac{3T}{4}$ e $t = T$

Surface stretching requires remeshing, which may also interfere on the volume conservation process. Regardless its volume conservation properties, any remeshing algorithm destroys the Lagrangian velocity history, requiring a new interpolation of the velocity field or the use of a first order scheme in the time step immediately after the remeshing operation. Since interpolation schemes are usually non-conservative, a conservative remeshing algorithm could still lead to a non-conserving volume outcome because of the need for velocity interpolation. In order to assess the influence of such variables on the volume of the Lagrangian interface, a series of tests was performed, in which three main parameters were analyzed: (i) the velocity field interpolation, (ii) the surface remeshing and (iii) the time integration scheme. The volumetric change was computed as a relative error, based on the initial sphere volume, according to Eq. (4.12):

$$\varepsilon = \left(1 - \frac{V_f}{V_i}\right) \times 100, \quad (4.12)$$

where V_i is the initial volume of the interface and V_f is the volume of the interface after finishing the shear flow. Table (4.4) shows the eight cases simulated.

Two sets of cases were run. In order to assess the influence of the velocity interpolation scheme on the conservation of volume, initially the velocity field was calculated directly on the Lagrangian interface. This was made in two cases: with and without surface remeshing. Therefore,

the influence of the remeshing algorithm on the volume change could also be tested. Then, a new set of tests was performed, but this time the velocity field was calculated on an auxiliary Eulerian framework and then interpolated to the Lagrangian interface. Again, this was performed with and without surface remeshing. The four cases described so far were simulated with no attempt to preserve the original volume, except for the volume-preserving features of the remeshing algorithm, as described in section 3.3.4.

In order to assess the ability of the volume recovery algorithm (described on section 3.3.2) on preserving the original interface volume, the cases described above were simulated again, but now with a volume-recovery step applied at the end of the of the advection of the surface, at each time step. The objective was to preserve the original volume of the interface, within a tolerance of $\pm 0.01\%$. Table (4.4) summarizes the case setup described above. In each of these cases, the simulation was performed with $dt = 0.001s$ and with $dt = 0.0005s$.

Table 4.4: Shear Flow. Case description for each test performed.

Case	Description		
	Volume Recovery	Velocity Interpolation	Remeshing
1	no	no	no
2	no	no	yes
3	no	yes	no
4	no	yes	yes
5	yes	no	no
6	yes	no	yes
7	yes	yes	no
8	yes	yes	yes

Figure (4.6) shows the volume change as a function of time for cases 1 to 4. The effect of surface remeshing can be assessed by comparing plots in the top of the figure with their corresponding ones on the bottom, while the effect of velocity interpolation appears when the plots on the left are compared with the plots on the right. Comparing cases 1 and 3 clearly shows the influence of the remeshing operation on the volume change, especially on the second order temporal scheme. Also, notice that although the error between the initial and final volume are negligible for the 2nd order scheme, it reaches a maximum value around 1% when $t = T/2$. The 1st order scheme, on the other hand, shows a cumulative trend in all cases. This cumulative behaviour also appears in the 2nd order scheme when surface remeshing is enabled, although with much smaller

intensity.

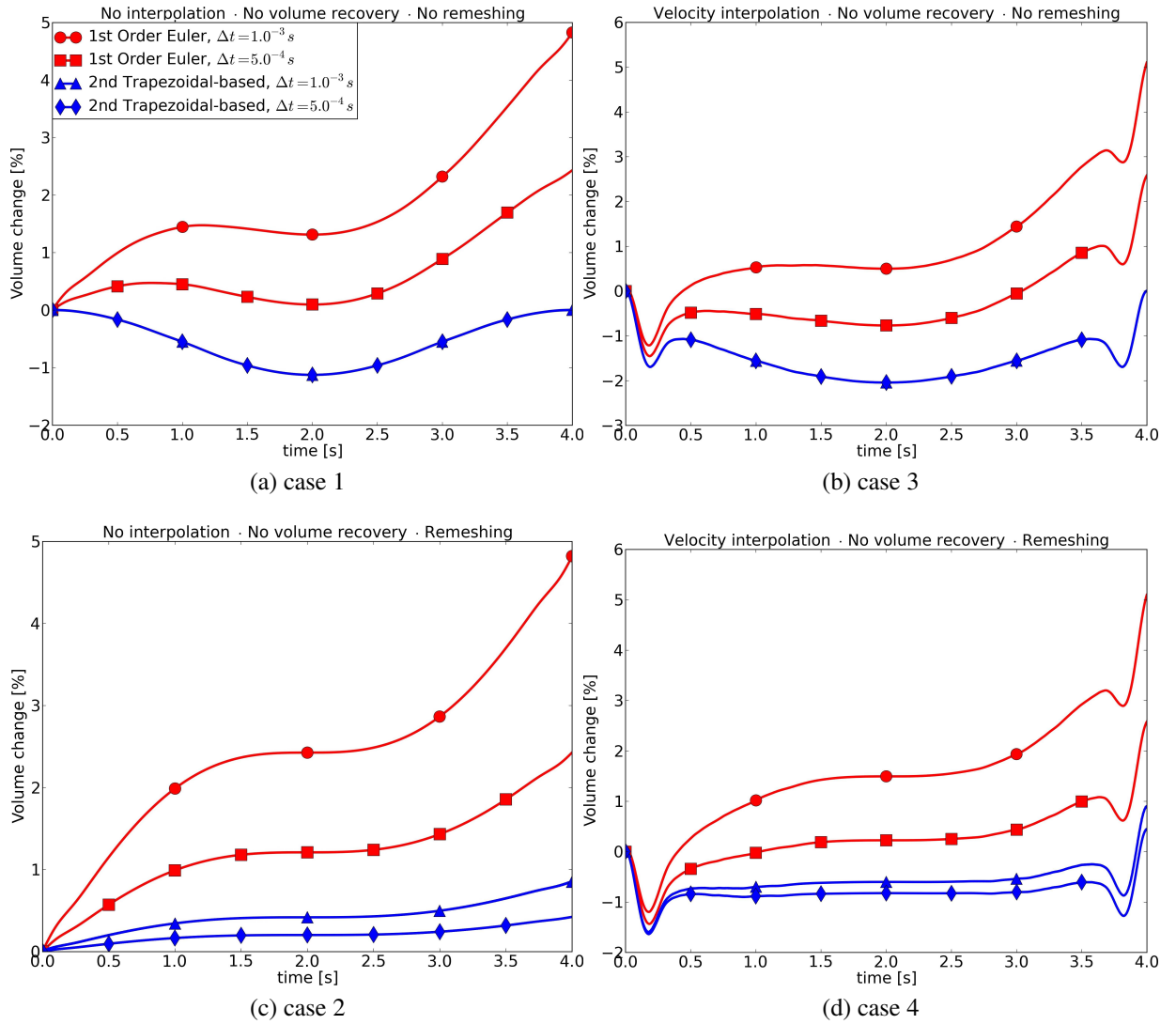


Figure 4.6: The influence of velocity interpolation and surface remeshing on the preservation of the initial interface volume.

Regarding the volume recovery algorithm, Fig. (4.7) shows that the volume change was successfully kept within the specified range of $\pm 0.01\%$ of the original volume.

4.1.3 Spurious currents

Spurious currents or parasitic currents are non-null velocity fields generated in static bubble flow simulations due to numerical errors caused by unbalance that arise during the surface force calculation (SINGH; SHYY, 2006). Tests for quantifying such currents consist in simulating a bubble or a droplet immersed in a flow with zero gravity and zero initial velocity field. In such

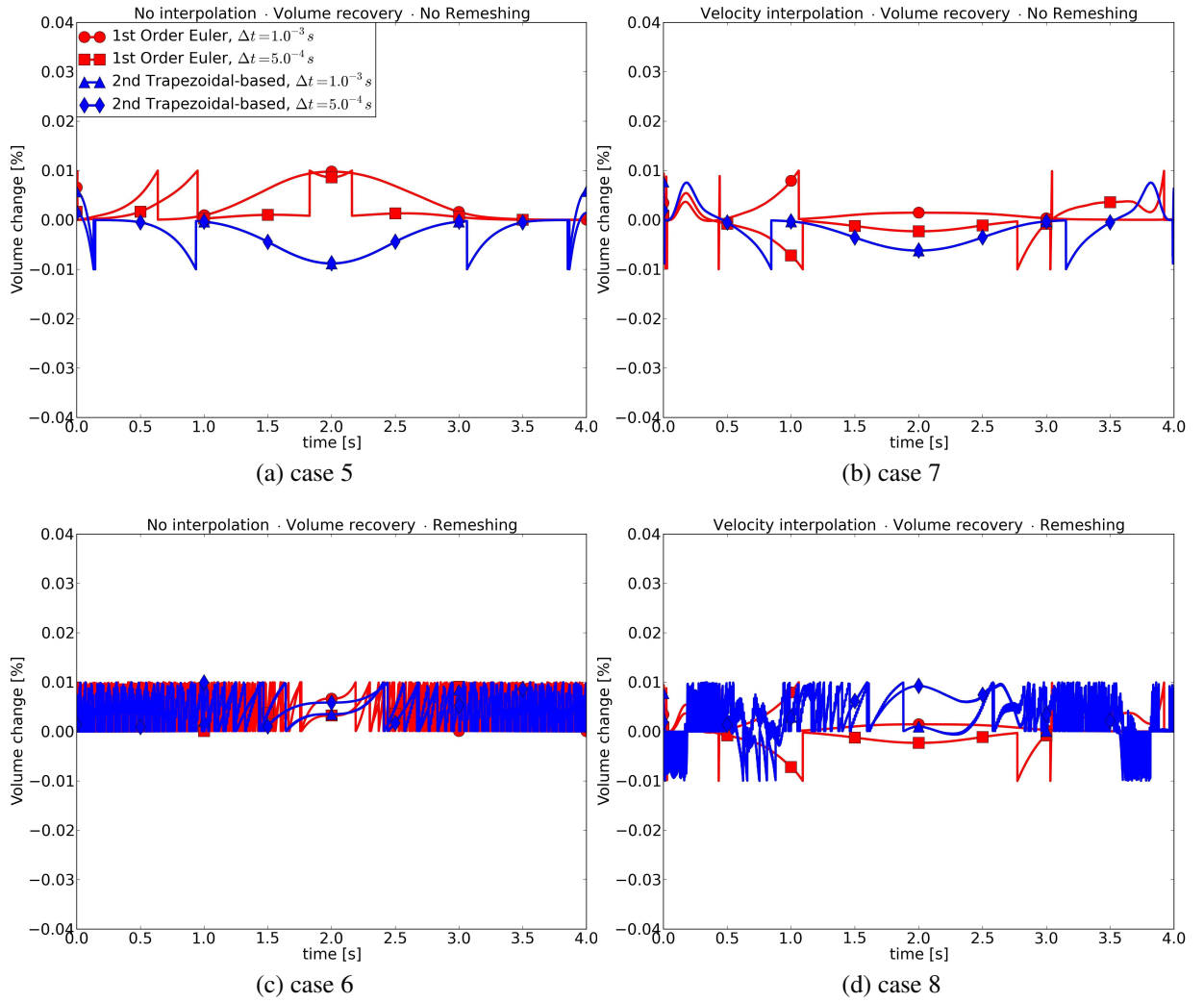


Figure 4.7: The influence of the volume recovery algorithm on the preservation of the initial interface volume.

situation the buoyancy force would be null and the bubble/droplet should stand still during the whole simulation.

The flow is characterized by two non-dimensional parameters: the Laplace (La) number and the Capillarity (Ca) number, respectively Eqs. (4.13a) and (4.13b):

$$La = \frac{\sigma \rho \phi}{\mu^2} \quad (4.13a)$$

$$Ca = \frac{\|u\|_{\infty} \mu}{\sigma} \quad (4.13b)$$

where σ is the interface tension coefficient, ρ is the density, ϕ is the sphere diameter, μ is the viscosity and $\|u\|_{\infty}$ is the maximum velocity magnitude found in the velocity field (SHIN; JURIC,

2002).

In order to assess the magnitude of the spurious currents in the present computer code, five cases were simulated, in which the Laplace number ranged from 1.2 to 12000. The results, presented in Table (4.5), show good agreement with (SINGH et al., 2005) and (SOUSA et al., 2004), who report Capillarity numbers $Ca = \mathcal{O}(10^{-4})$.

Table 4.5: Capillarity number as a function of the Laplace number.

La	Ca
1.2	9.84×10^{-4}
12	1.17×10^{-3}
120	1.08×10^{-3}
1200	1.09×10^{-3}
12000	8.76×10^{-4}

4.2 Rising Bubbles

4.2.1 Introduction

After the verification tests presented in the previous section, the implementation of the numerical method is thoroughly tested for the simulation of a single rising bubble ascending in various regimes. Initially, a sensitivity analysis was performed, with two objectives: to assess (i) the role of some geometric parameters and (ii) the influence of the density ratio on the outcome of the flow. The results obtained in this analysis were applied in the setup of the forthcoming cases, which were mainly based on (BHAGA; WEBER, 1981) and (HUA; LOU, 2007). In the first group of cases, the ability of the method for simulating different bubble regimes was studied. The second group simulated a series of cases in which the bubbles have the same Eotvos number (Eo), in order to study the influence of the Morton number (M) on the Reynolds (Re) profile. A third group was simulated aiming at comparing the streamline pattern obtained in this work against the aforementioned references. Finally, some wobbling simulations were performed, based on the works of (STENE, 2010). In all cases, the following boundary conditions were applied:

- Velocity

free-slip at the side boundaries (homogeneous Dirichlet at the normal direction and homogeneous Neumann at the tangential direction);

homogeneous Dirichlet at the bottom boundary;

homogeneous Neumann at the top boundary.

- Pressure

homogeneous Neumann at the side and bottom boundaries

homogeneous Dirichlet at the top boundary.

Figure (4.8) (CLIFT; GRACE; WEBER, 1978) shows the location of the cases simulated in this work inside the Clift diagram.

Two parameters were used for flagging the regions of the Eulerian domain for grid refinement: the position of the Lagrangian interface and the vorticity magnitude. In all cases simulated, the grid spacing at the finest level was set to $\phi/32$. In the cases of sections 4.2.2 and 4.2.3, five levels of refinement were used. The dimensions of the Eulerian domain were set to $(8\phi \times 8\phi \times L_z)$, and different values were used for the z-dimension: $L_z = 16\phi$ (cases A1-A11), $L_z = 24\phi$ (density ratio) and $L_z = 80\phi$ (wobbling). Therefore, an uniform grid with the same grid spacing would have approximately 3.355×10^7 cells for the first case and 1.678×10^8 on the last case. On the other hand, adaptive grids required, on average, 100 times less. Details about the grid sizes will be presented during the description of each case.

4.2.2 Sensitivity Analysis

Several geometry-related parameters may influence the outcome of the simulation. In this section these parameters will be studied, based on the simulation of a bubble rising in a quiescent liquid in the spherical cap regime, as suggested by Lemonnier, Jamet and Lebaigue (2005): $Eo = 40$, $M = 0.056$, $\rho_C = 1000 \text{ kg/m}^3$, $\mu_C = 0.273556 \text{ Pa} \cdot \text{s}$, $\lambda_\rho = 100$, $\lambda_\mu = 100$. The bubble diameter is $\phi = 0.02 \text{ m}$ and the terminal Reynolds is $Re = 20.6$. ρ_C and μ_C are the density and dynamic viscosity of the continuous phase and λ_ρ and λ_μ are the density ratio and viscosity ratio between the continuous and dispersed phase, respectively. On all cases run in this sensitivity analysis, the

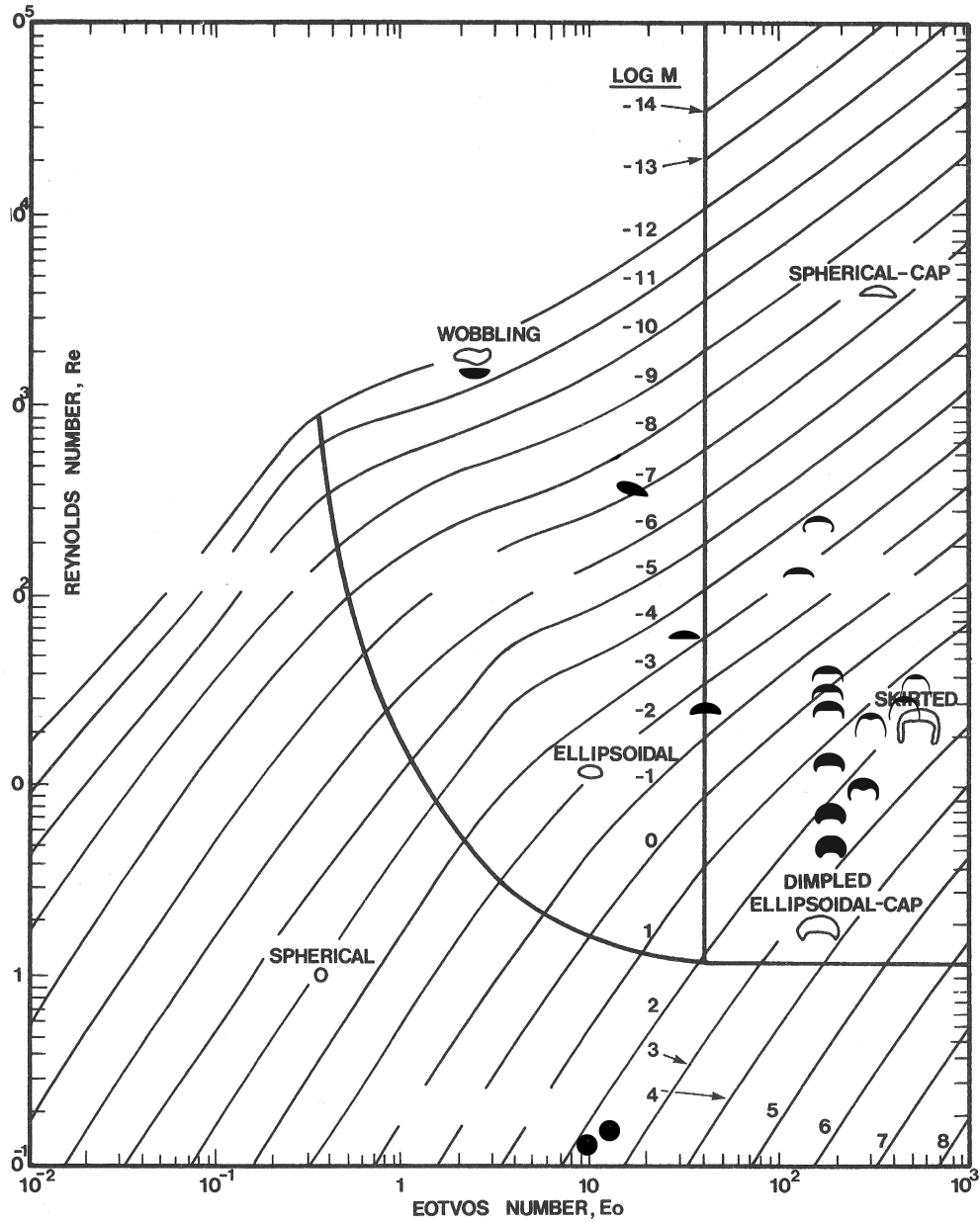


Figure 4.8: Clift Diagram (CLIFT; GRACE; WEBER, 1978) and the cases simulated in this work (bubble shapes shown in black).

difference between the present work and the aforementioned reference work is quantified by the relative error based on the terminal Reynolds number.

Four cases were run in order to assess the role of the geometric correction tools on the flow simulation. In case A1 the standard Front Tracking Method was used, without any further intervention. In case A2 a volume correction step was applied at the end of the interface advection, while in case A3 only TSUR3D was used. Case A4 applies both, volume recovery and TSUR3D algorithms. The effect of the geometric tools on the Re number and terminal velocity on each case is shown in Table (4.6), which quantifies the errors based on (LEMONNIER; JAMET; LEBAGUE,

2005).

Table 4.6: A-series: Cases description and error on the terminal Re number. Reference $Re = 20.6$.

Case	Description	Re	Relative Error (%)
A1	Standard Front Tracking Algorithm	23.5	12.3
A2	A1 + Volume Recovery	23.3	11.6
A3	A1 + Wrinkle removal	19.9	3.5
A4	A1 + Volume Recovery + Wrinkle Removal	19.8	4.0

Figure (4.9) shows the time evolution of the Reynolds number and Fig. (4.10) shows the terminal bubble shape and relative position in the first and in the last time step for each case. Notice that the volume recovery algorithm has little influence at the beginning of the flow. In fact, only after reaching the terminal regime a small decrease in the Re number can be seen. Surface wrinkle removal, on the other hand, affects the early stages of the flow by smoothing the transient region and decreasing the Re maximum at the overshoot region. Since the volume is conserved along the simulation, the changes in Reynolds number comes from the bubble ascending velocity, which is clearly shown in Fig. (4.10).

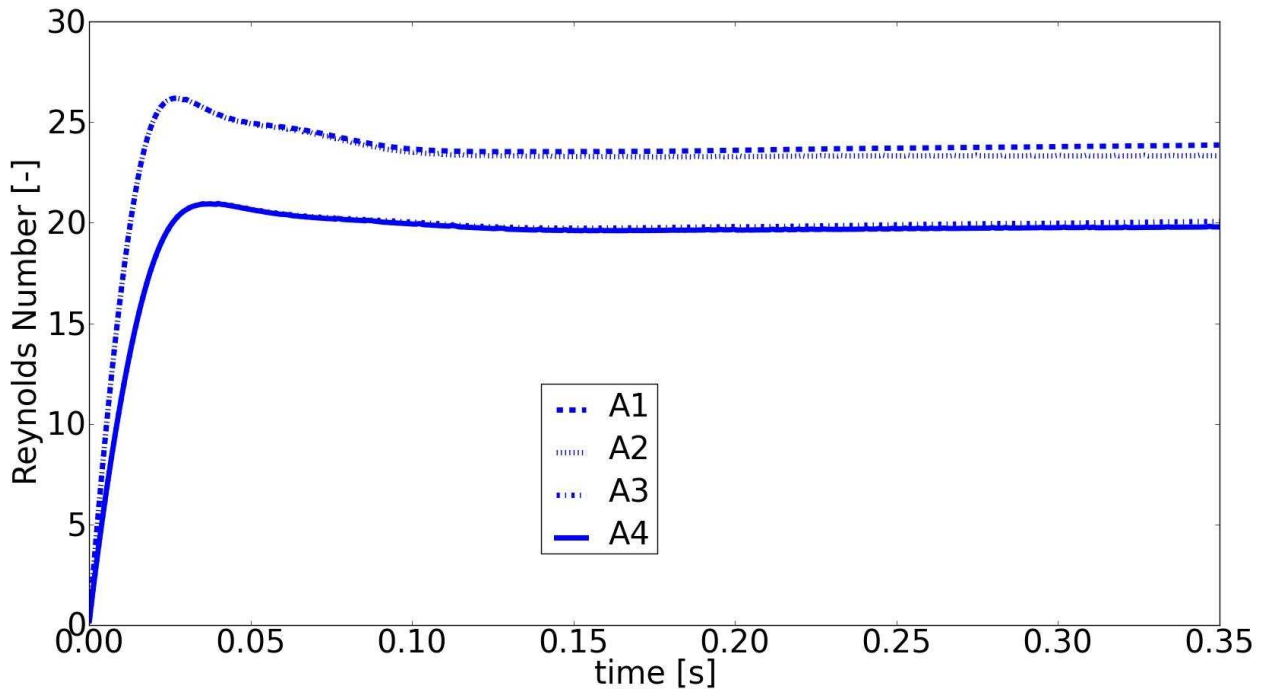


Figure 4.9: A-series: Terminal Reynolds number depending on the geometric intervention applied. Reference Reynolds number: $Re = 20.6$.

The temporal evolution of the wrinkles is shown in Fig. (4.11), and Fig. (4.12) shows details of the bubble shape at the end of the flow for cases A1 and A3. Figure (4.13) shows that

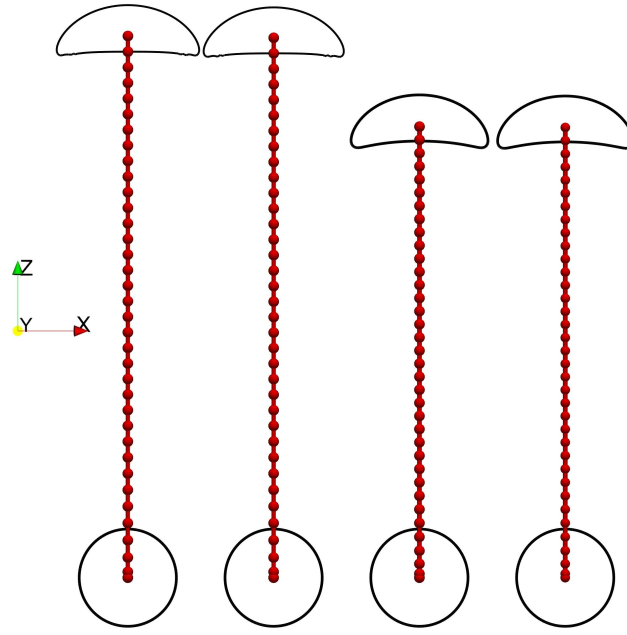


Figure 4.10: A-series: Bubble shape and relative position at the beginning and at the end of the simulation, depending on the geometric intervention applied. From left to right: cases A1, A2, A3 and A4.

the presence of the wrinkles lead to the formation of artificial vortices on the bubble rear.



Figure 4.11: A-series: Temporal evolution of wrinkles when no smoothing procedure is applied. From left to right: $t = T/2$, $t = T/4$, $t = 3T/4$, $t = T$.

Domain Size

In order to assess the influence of the domain size on the bubble shape and position, as well as on the terminal Reynolds number, four cases were simulated. Assuming gravity acting on the $-z$ direction and a square cross-section in the xy plane, Table (4.7) shows the domain sizes used in the simulation, the terminal Re obtained and the associated relative errors. Volume recovery and wrinkle removal algorithms were applied to all cases.

Figure (4.14) shows the relative position of the bubble at the end of the simulation for all

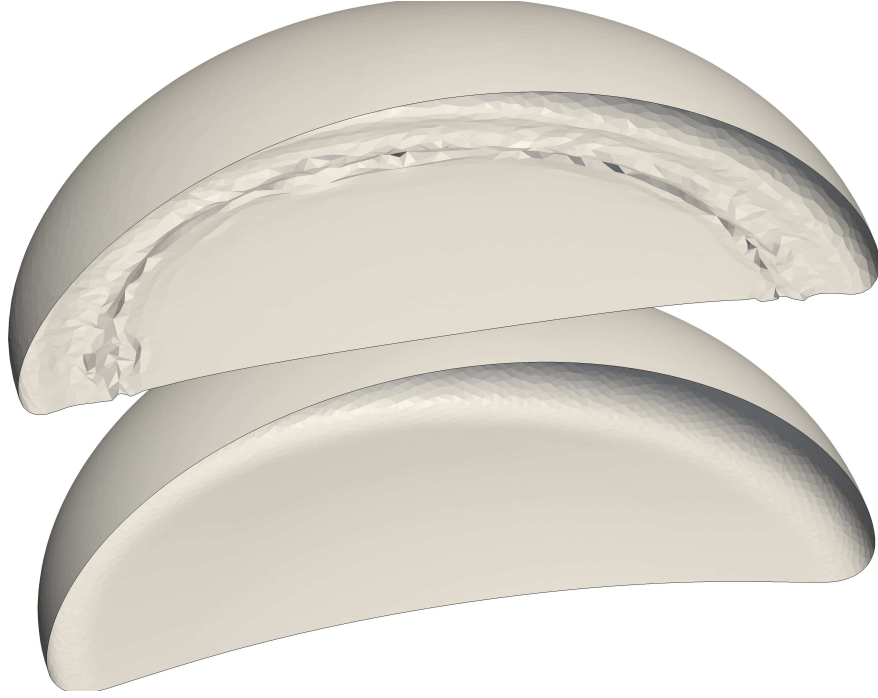


Figure 4.12: Bubble shape at the end of the simulation. Top: no geometric intervention. Bottom: volume recovery and wrinkle removal.

Table 4.7: Influence of the domain size on the terminal Reynolds number. All cases were run with $L_z = 16\phi$. Reference $Re = 20.6$.

Case	$L = L_x = L_y$	Centre	Re	Error (%)
A5	$L = 4\phi$	$(2\phi, 2\phi, 2\phi)$	18.9	8.25
A6	$L = 6\phi$	$(3\phi, 3\phi, 2\phi)$	19.6	4.85
A7	$L = 8\phi$	$(4\phi, 4\phi, 2\phi)$	19.8	4.0
A8	$L = 10\phi$	$(5\phi, 5\phi, 2\phi)$	19.9	3.5

cases, whereas Fig. (4.15) shows the Re profile for each simulation. Figure (4.15) shows that a domain with cross-section $L = 4\phi$ still has some influence on the bubble rising velocity. Table (4.7) shows an error $\varepsilon = 8.25\%$ for this case, whereas the other 3 cases yielded errors around 4%. Since volume recovery and wrinkle removal algorithms were applied on all cases, no sensible difference in shape or volume was found between the cases. Case A7 was chosen as a commitment solution between the low cost of domain A6 and the larger domain A8, which yields more details about the flow at the cost of time and computer efforts.

Resolution of the Eulerian Mesh

In order to assess the sensitivity of the flow solution to the Eulerian grid resolution, case A4 was simulated using three different grid resolutions: $\phi/16$, $\phi/32$ and $\phi/64$. Since no significant

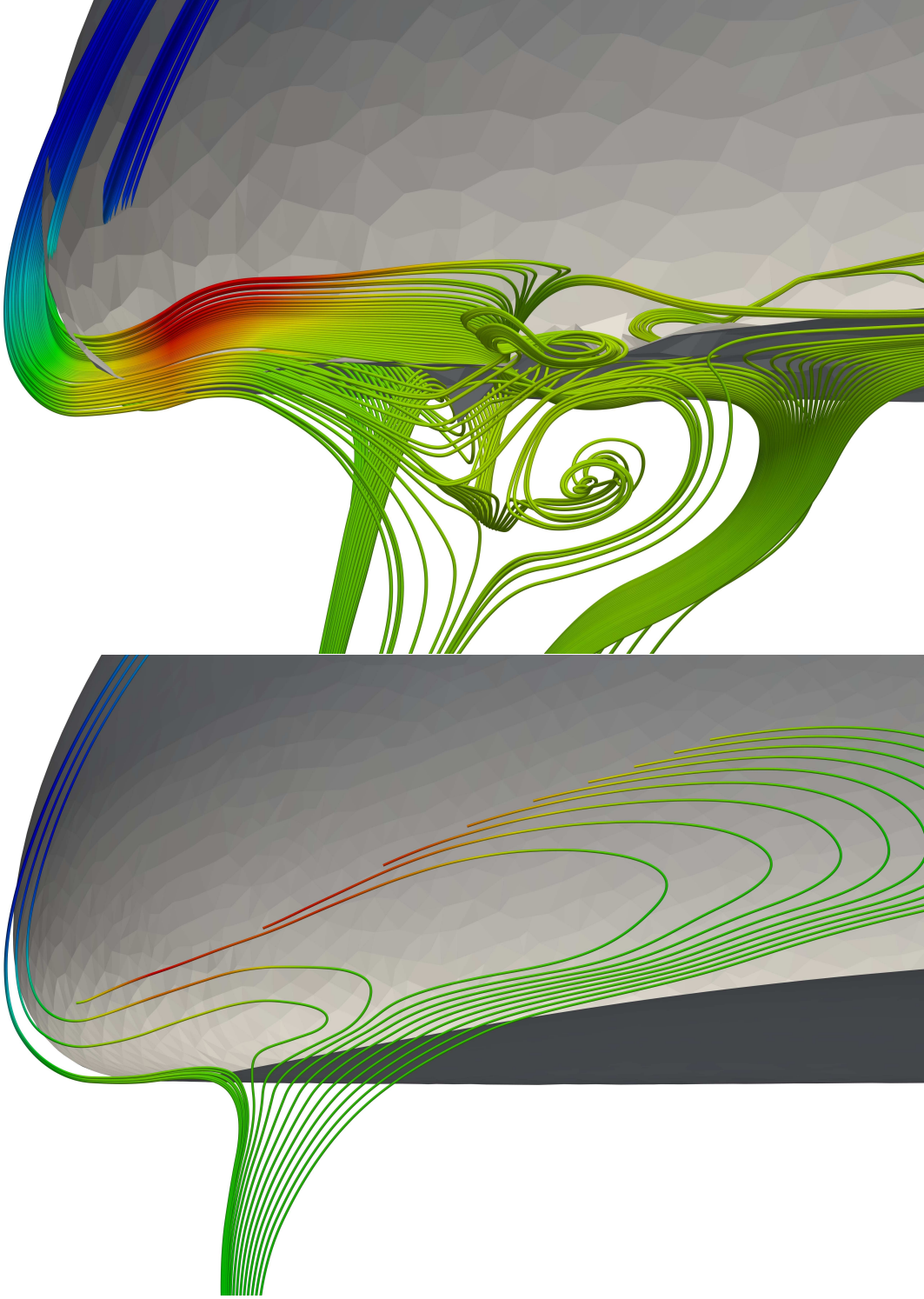


Figure 4.13: A-series: Streamlines inside and at the rear of the bubble. Top: no geometric intervention. Bottom: volume recovery and wrinkle removal.

change in the error was detected and the computational cost (in terms of wall time) for the third case was about five times higher than the second case, the grid resolution $\phi/32$ was adopted as the standard grid refinement for all cases, along with a domain size $Lx = Ly = 8\phi$, $Lz = 24\phi$.